CHEMISTRY OF MATERIALS

Article

pubs.acs.org/cm

Scalable Solution-Grown High-Germanium-Nanoparticle-Loading Graphene Nanocomposites as High-Performance Lithium-Ion Battery Electrodes: An Example of a Graphene-Based Platform toward Practical Full-Cell Applications

Fang-Wei Yuan and Hsing-Yu Tuan*

Department of Chemical Engineering, National Tsing Hua University, 101, Section 2, Kuang-Fu Road, Hsinchu, Taiwan 30013, Republic of China

Supporting Information

ABSTRACT: Graphene in the form of graphene/nanocrystal nanocomposites can improve the electrochemical performance of nanocrystals for lithium-ion (Li-ion) battery anodes, which is especially important for high-capacity Li-alloy materials such as Si and Ge. For practical full-cell applications, graphene composite electrodes consisting of a large portion of active materials (i.e., a surface of graphene sheets evenly distributed with dense nanoparticles) are required. We have developed a facile solution-based method to synthesize subgram quantities of nanocomposites composed of reduced graphene oxide (RGO) sheets covered with a high concentration (~80 wt %) of single-crystal 4.90(±0.80) nm diameter Ge nanoparticles. Subsequently, carbon-coated Ge nanoparticles/RGO (Ge/RGO/C) sandwich structures were formed via a carbonization process. The high-nanoparticle-loading nanocomposites exhibited superior Li-ion battery anode performance when examined with a series of comprehensive tests, such as receiving a practical capacity of Ge (1332 mAh/g) close (96.2%) to its theoretical value (1384 mAh/g) when cycled at a 0.2 C rate and having a high-rate capability over hundreds of cycles. Furthermore, the performance of the full cells assembled using a Ge/RGO/C anode and an $LiCoO_2$ cathode were evaluated. The cells were able to power a wide range of electronic devices, including an light-emitting-diode (LED) array consisting of over 150 bulbs, blue LED arrays, a scrolling LED marquee, and an electric fan. Thus, this study demonstrates a proof of concept of the use of graphene-based nanocomposites toward practical Li-ion battery applications.

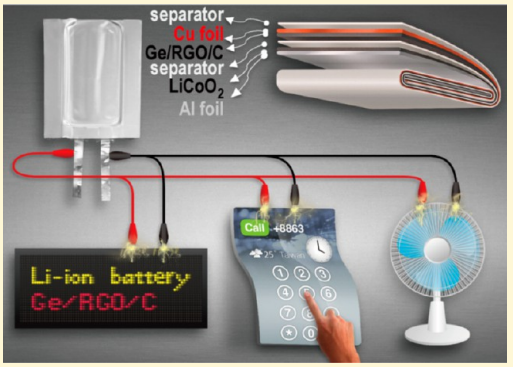

1. INTRODUCTION

Lithium-ion (Li-ion) batteries are used to power most portable electronic products because of their attractive, advantageous properties, such as a high working voltage, a high energy density, portability, low-maintenance care, long cycle and shelf life, and no memory effect.[1−10] A standard Sony 18650 battery consists of an $LiCoO_2$ cathode and a graphite anode that have theoretical capacities of 274 and 372 mAh/g, respectively.[11−13] However, current designs do not meet urgent requirements of more advanced applications, such as lighter, more durable consumer electronics, electric care, and energy storage for green grids that require higher energy and power density. The direct way to increase the battery capacity is to replace the electrode materials with other materials having larger Li-storage capacity. For example, in an 18650 cell, if graphite is replaced with an anode material having a capacity greater than 1000 mAh/g, then more than a 20% increase in total capacity can be obtained.[14] Therefore, Li-alloy-based materials with high degrees of lithiation, especially for Si and Ge, are considered to be attractive alternatives to graphite.[15−28] However, bulk Li-alloy-based anodes exhibit rapid capacity fading after several cycles because of dramatic volume changes (e.g., ~300% for Si and Ge) resulting from the insertion/extraction of Li ions.[14,17] Although nanoparticles of Li-alloy-based materials can tolerate mechanical stress to exhibit improved performance, they usually suffer from poor capacity retention after tens of cycles.

Recent studies have shown that a wide range of graphene/nanoparticles nanocomposites exhibit significantly improved electrode performance relative to the original performance of the nanparticles themselves.[29−31] Graphene has a large specific surface area (up to 2630 m^2/g) for immobilization of nanoparticles, excellent mechanical properties (1060 GPa) against distortion, and excellent electrical conductivity for Li-ion transport.[32−36] Furthermore, nanoparticles stabilized on graphene sheets can significantly reduce the level of aggregation resulting from the insertion/extraction of Li ions. Nonetheless, there still appears to be challenging issues in incorporating graphene-based materials into practical battery systems. One major concern is that composites usually contain a large portion of graphene and give rise to a lower compact density because of

Received: January 19, 2014
Revised: February 11, 2014
Published: February 13, 2014

   dx.doi.org/10.1021/cm5002016 | Chem. Mater. 2014, 26, 2172−2179

their large surface-to-volume ratio. Therefore, to obtain higher-output electrode capacity, it is highly desirable to fabricate graphene sheets attached with a large amount of nanoparticles and to subsequently cover them densely on copper foil to prepare anodes. However, high-nanoparticle-loading graphene nanocomposites usually exhibit poor long-term cycle stability (e.g., over 100 cycles) because nanoparticles do not anchor tightly and tend to aggregate on graphene sheets. This situation occurs particularly at charge/discharge rates greater than 1 C. Therefore, it is essential to obtain the best compromise for the amount of nanoparticle supported on graphene. More importantly, the demonstration of graphene-based nanocomposites applicable for practical Li-ion applications is required, but it has been rarely addressed in most of the literature.

In this study, high-nanoparticle-loading (~80 wt %) graphene nanocomposites were synthesized and employed as Li-ion battery anodes and comprehensively examined for their performance evaluation in both half cells and full cells. Here, germanium (Ge) was chosen as the nanocrystal system because it has a high theoretical capacity of 1384 mAh/g at room temperature ($Li_{15}Ge_4$ phase), fast diffusion rate of Li ions, and high operating voltage rates. Scheme 1 illustrates the overall

Scheme 1[a]

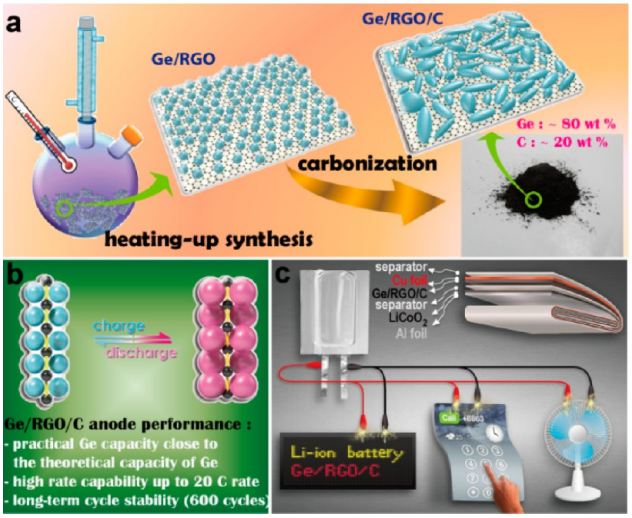

[a](a) Illustration of the preparation process for high-nanoparticle-loading Ge/GRO/C nanocomposites. (b) Scheme of the structure evolution of Ge/RGO/C nanocomposites between charge/discharge cycles. (c) Illustration of aluminum-pouch-type Li-ion batteries using a Ge/RGO/C as the anode and an $LiCoO_2$ as the cathode for powering different portable devices.

presentation and major ideas of this work. First, a solution-based heating-up method was developed to synthesize subgram quantities of Ge/reduced graphene oxide (Ge/RGO) nanocomposites. Single-crystal Ge nanoparticles with an average diameter of 4.90(±0.80) nm were densely grown on RGO sheets via one-pot growth. After a carbonization process, carbon-coated Ge/RGO (Ge/RGO/C) sandwich structures with ~80 wt % Ge nanoparticles were formed and shown to exhibit excellent anode performance. Second, the electrodes exhibited excellent electrochemical performance, with a reversible capacity of 1166 mAh/g when cycled at a 0.2 C rate (1 C = 1 A/g), corresponding to the practical capacity of Ge as high as 1332 mAh/g, which is very close (96.2%) to the theoretical capacitance of Ge. The electrodes exhibit long cycle life high-rate capabilities, with nearly 100% capacity retention after cycling 600 times at a 1 C rate and 300 times at a 2 C rate. Additionally, the electrodes were evaluated in a 500-cycle test with cycle rates ranging from 0.2 to 20 C, where a reversible capacity of 720 mAh/g at a rate of 20 C was achieved. Finally, the performance of full cells assembled with the Ge/RGO/C as the anode and $LiCoO_2$ as the cathode was evaluated, and their applications for powering a wide range of electronic devices were shown.

2. EXPERIMENTAL SECTION

2.1. Materials. Graphite (Bay Carbon, SP-1, 200 mesh), pottasium permanganate ($KMnO_4$, J. T. Baker, 99%), sodium nitrate ($NaNO_3$, J. T. Baker, 99%), hydrogen peroxide (H_2O_2, Aldrich, 30%), sulfuric acid (H_2SO_4, Alfa Aesar, 95–97%), oleylamine ($CH_3(CH_2)_7CH{=}CH(CH_2)_7CH_2NH_2$, Aldrich, 70%), germanium(II) iodide (GeI_2, Aldrich, ≥99.9%), toluene (J. T. Baker, 99%), and ethanol (C_2H_5OH, Aldrich, 99.8%) were purchased as indicated. $LiPF_6$ (1.0 M in a 1:1 mixture of ethylene carbonate/dimethyl carbonate), Celgard membrane (as separator), Li metal foil (99.9%), Cu metal foil (0.01 mm), $LiCoO_2$ cathode electrode, PVDF, NMP (99%) super-p carbon black, and coin-type half-cells (CR2032) were purchased from SYNergy ScienTech Corp. LEDs were purchased from an electronic equipment and appliance store.

2.2. Preparation of GO Nanosheets. GO nanosheets were prepared by oxidation and exfoliation of commercially available graphite by Hummers method. 0.5 g of natural graphite (Bay Carbon, SP-1) and 0.5 g of sodium nitrate were mixed in a 500 mL round-bottomed flask. Concentrated sulfuric acid was then added to the mixture under ice-bath cooling. Upon reaching 0 °C, 3 g of potassium permanganate was slowly added to the cooled acid solution mixture, and the whole pot was transferred to a warm water bath (~40 °C). After stirring for 1 h, 30 mL of deionized (DI) water was added to the solution and left stirring for another 30 min, after which it was further diluted by 100 mL of deionized water. Following the dilution, 3 mL of hydrogen peroxide was added dropwise into the solution. The solution was filtered and washed until the filtrate became pH neutral. The filter cake was redispersed in 100 mL of DI water and sonicated for 30 min for the exfoliation of graphite oxide. The dispersion was then subjected to 8000 rpm centrifugation for 15 min, and the sediment was collected. The sediment was again redispersed in DI water and subjected to 1000 rpm centrifugation for 2 min, and the sediment was discarded (note that this step was repeated for 3–5 times until there was no visible particulate). The dispersion was centrifuged at 8000 rpm for 15 min to collect the final exfoliated GO product, which was oven-dried and kept for functionalization and characterization.

2.3. Functionalization of GO. 5 mL of oleylamine and 15 mL of toluene were added to 20 mg of oven-dried GO. Subsequently, the mixture was sonicated for 30 min until GO was homogeneously dispersed in the solution, and the dispersion was then centrifuged at 8000 rpm for 15 min to collect the sediment. The sediment, referred to as oleylamine-GO, was redispersed in 40 mL of oleylamine and kept as the stock solution.

2.4. Preparation of Ge/RGO and Ge/RGO/C Nanocomposites. In a typical synthesis, 0.5 g of GeI_2, 35 mg of oleylamine stabilized-GO, and 50 mL of oleylamine were added to a 100 mL three-necked flask in a glovebox. One neck of the flask was connected to a thermocouple for temperature monitoring control; the other neck was sealed by a rubber septum. After removed from the glovebox, the third neck of the flask was quickly connected to the Schlenk line. Next, the temperature of the mixture was increased to 275 °C at a ramping rate of 15 °C/min. The reaction was held at 275 °C for 3.5 h with continuous vigorous stirring, resulting in a dark brown colloidal solution. The reaction was allowed to cool to room temperature, and the Ge/RGO composites were flocculated by adding 5 mL of ethanol and 35 mL of toluene, which was collected by centrifugation at 8000 rpm for 5 min. After a washing step, the Ge/RGO composites were in

dx.doi.org/10.1021/cm5002016 | Chem. Mater. 2014, 26, 2172–2179

the precipitate, whereas the supernatant containing unreacted precursors and byproducts was discarded. The Ge/RGO/C composites were prepared under a 5% H_2/95% Ar atmosphere at 500 °C for 2 h in a furnace to obtain a dark powder. Both the Ge/RGO and Ge/RGO/C nanocomposites were stored in a glovebox for further characterization and application.

2.5. Characterization. All products were characterized using scanning electron microscopy (SEM) and transmission electron microscopy (TEM). For HRSEM imaging, images were obtained using a SEM operated at a 5−15 kV accelerating voltage with working distances ranging between 10 and 20 mm. The TEM samples were prepared by drop-casting the composites from toluene dispersions onto 200-mesh lacey carbon-coated copper grids (Electron Microscope Sciences). Images were acquired using a 200 kV accelerating voltage on a JEOL JEM-2100F and a 300 kV accelerating voltage on a JEOL JEM-3000F, all equipped with an Oxford INCA EDS spectrometer. For conducting ex situ TEM analysis of the samples after charge/discharge tests, the composite electrode was dissembled from the cell and dispersed in acetone with ultrasonic treatment. The carbon content of the composites was characterized using a Heraeus varioIII-NCH.

2.6. Li-Ion Battery Assembly and Electrochemical Characterization. The composite electrode was prepared by mixing active materials (75 wt %) with 10 wt % of super-p carbon black and 15 wt % of PVDF binder in NMP solvent to form a homogeneous slurry, which was then spread onto a copper foil. The weight of pure active material was measured using a microbalance with 0.1 μg resolution (Sartorius SE2). Typical anode mass loading was ~0.6 mg/cm^2. The electrodes were dried at 40 °C in air and then at 150 °C under Ar gas prior to cell assembly to remove any residual water. The coin-type half-cells (CR2032), prepared in an argon-filled glovebox, contained a composite electrode, Li metal foil, and microporous polyethylene separator soaked in electrolyte. The electrolyte solution was 1 M $LiPF_6$ in ethylene carbonate/dimethyl carbonate (EC/DMC) (1:1 v/v). The aluminum-pouch-type Li-ion batteries were prepared using a commercial full-cell assembly line (SYNergy ScienTech Corp). The cathode electrode, separator, and anode electrode were first rolled to a suitable size (scheme 1c), after which the electrodes were assemble with an aluminum bag. The electrochemical performance of the Ge nanowires was evaluated using Biologic VMP3 instruments. For full-cell assembly, the $LiCoO_2$ electrode with a loading mass of ~7 mg/cm^2 was used as a cathode, whereas the anode mass loading was kept at ~0.6 mg/cm^2. The electrochemical properties of the CR2032 full cells were examined at a 1 C rate in voltage windows between 2.5 and 4.2 V with the same experimental system. The electrode capacity was calculated according to the weight of the active materials.

3. RESULTS AND DISCUSSION

Synthesis of Ge/RGO nanocomposites was carried out in heating-up reactions by decomposition of GeI_2 precursor at 275 °C in the presence of oleylamine-functionalized GO. Ge nanoparticles nucleated on both sides of the GO sheets during the synthesis, and the GO was synchronously reduced to RGO by oleylamine at elevated temperatures. X-ray diffraction (XRD) of the product in powder form showed diffraction peaks at 27.3, 45.3, 53.8, 66.0, and 72.8°, which can be indexed to the standard cubic phase of Ge crystals in the JCPDS database (see Figure S1 in the Supporting Information).[37] In addition, the SEM images of the Ge/RGO nanocomposites show that the lateral size of the graphene sheet is mostly greater than 10 μm (Figure 1b,c). The TEM images that show the Ge nanoparticles are densely and uniformly covered on the surface of graphene sheets (Figure 1d,e), and the HRTEM image (Figure 1f) of the Ge nanoparticles shows their single-crystal nature with an average diameter of 4.90(±0.80) nm (the measured size distribution is shown in Figure 1h). The selected-area electron diffraction (SAED) pattern of the Ge

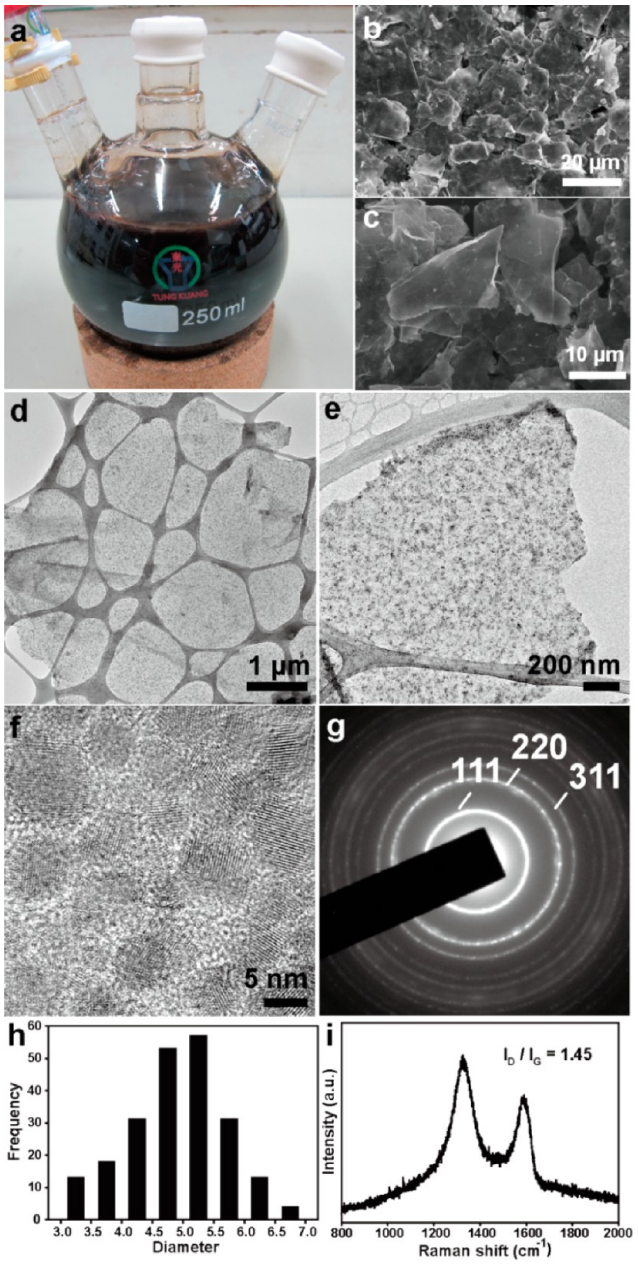

Figure 1. (a) Photograph of Ge/RGO nanocomposite product in a 250 mL three-necked flask obtained from a heating batch reaction. (b, c) SEM images, (d, e) TEM images, and (g) SAED pattern of Ge/RGO nanocomposites. (h) Size distribution of Ge nanoparticles on the surface of RGO sheets. (i) Raman spectra of Ge/RGO nanocomposites.

nanoparticles on the RGO sheets (Figure 1g) corresponds to the specific crystalline planes of Ge.[38] The synthetic protocol can produce subgram quantities of Ge/RGO products. The amount of carbon in the composites was about 22.02 wt %, as measured with a CHNS analyzer (Table S1 in the Supporting Information). Figure 1a shows subgram scale synthesis of Ge/RGO nanocomposites from a batch reaction in a 250 mL three-necked flask.

Ge/RGO/C nanocomposites were prepared with a carbonization process conducted at 500 °C in a 5% H_2/95% Ar atmosphere for 2 h. As confirmed by XRD, no discernible difference was observed before and after carbonization (see Figure S1 in the Supporting Information). Figure 2a shows the

dx.doi.org/10.1021/cm5002016 | Chem. Mater. 2014, 26, 2172−2179

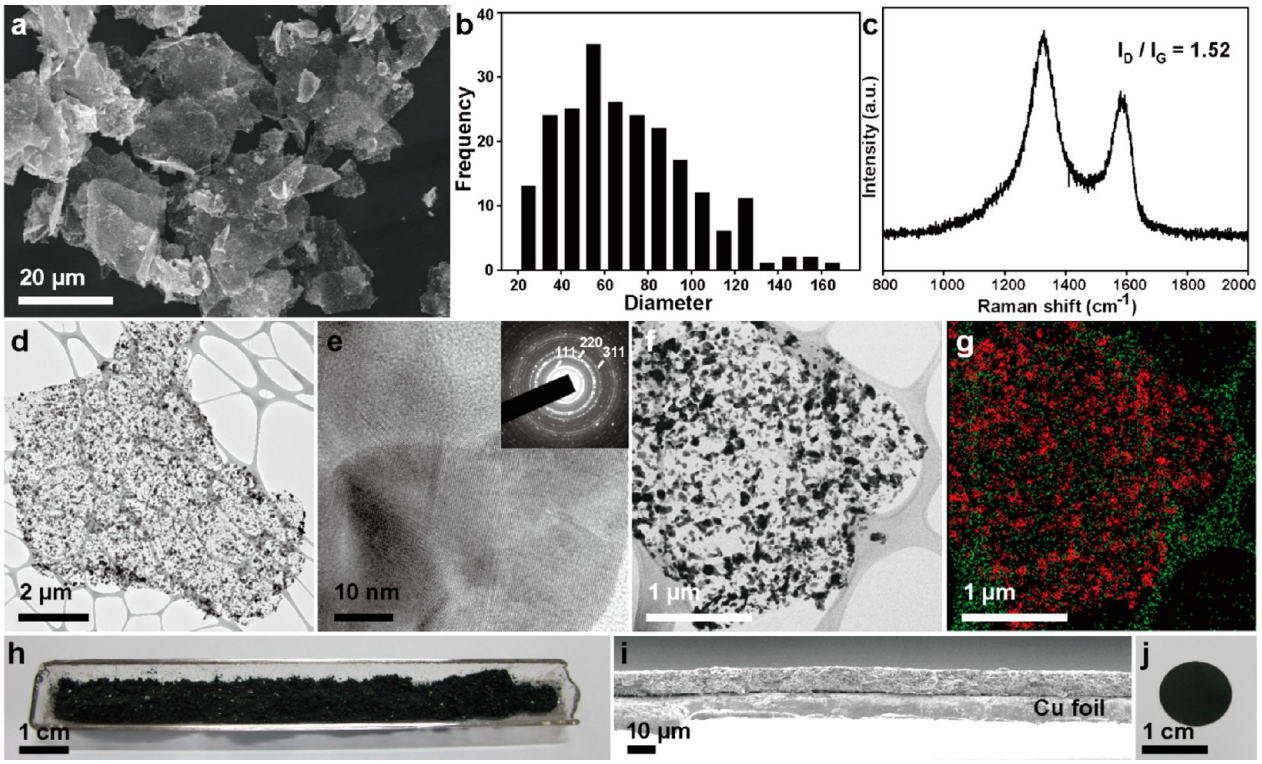

Figure 2. (a) SEM image of the carbonized Ge/RGO/C nanocomposites. (b) Size distribution of Ge nanoparticles on the surface of RGO sheets. (c) Raman spectra of the Ge/RGO/C nanocomposites. (d, e) TEM images and SAED pattern (inset in panel e is of the Ge/RGO/C nanocomposites). (f, g) STEM–EDS mapping profile of Ge (red) and C (green) in the composites. (h) Photograph of 0.6 g carbonized Ge/RGO/C nanocomposites. (i) Side-view SEM image of the composite electrode. (j) Photograph of Cu foil coated with a uniform layer of anode film.

SEM image of the Ge/RGO/C nanocomposites. The lateral dimension of the graphene sheet is similar to that of Ge/RGO; however, larger bright dots were observed on the surfaces of graphene sheets in the nanocomposites. The TEM images of the Ge/RGO/C nanocomposites clearly show the size increase of Ge nanoparticles, with a characteristic size of 70 ± 30 nm and polycrystalline nature (Figures 2d, 2e, and S2 in the Supporting Information). The carbon content in the nanocomposites was approximately 19.88 wt % (see Table S1 in the Supporting Information). Moreover, the Raman spectra of Ge/RGO (Figure 1i) and Ge/RGO/C (Figure 2c) show peaks at ~1592 cm^{-1} (G band), corresponding to the vibration of sp^2-bonded carbon atoms in a 2D hexagonal lattice, and 1334 cm^{-1} (D band), which is related to the defects and disorder in the hexagonal graphitic layers.[39,40] The intensity ratio of D band to G band, I_D/I_G, of Ge/RGO was calculated to be 1.45, whereas the calculated ratio of Ge/RGO/C increases to 1.52. This increase can be attributed to amorphous carbon coating because of oleylamine decomposition at 500 °C, suggesting the formation of sandwich structures. Moreover, scanning transmission electron microscope–energy-dispersive X-ray spectroscopy (STEM–EDS) mapping was performed to show the homogeneous distribution of Ge on the graphene sheets (Figure 2f,g). The anodes were fabricated by mixing Ge/RGO/C with poly(vinylidene fluoride) (PVDF) binder and carbon black in *N*-methyl-2-pyrrolidinone (NMP). The composite electrodes form on copper foil after the removal of NMP under overnight mild heating (Figure 2j). The thickness of the Ge/RGO/C anode is ~10 μm, and the mass density loading is ~0.6 mg/cm^2 (Figure 2i).

The electrochemical performance of Ge/RGO/C was evaluated with charge/discharge galvanostatic cycles in a CR2032 coin cell using Li metal as the counter electrode between 0.01 and 1.5 V. Figure 3a shows the galvanostatic cycling results at a rate of 0.2 C. The first discharge/charge cycle delivers a specific charge capacity of 2302 mAh/g and a discharge capacity of 988 mAh/g, corresponding to a Coulombic efficiency of 43%. This initial capacity loss can be attributed to the formation of a solid electrolyte interphase (SEI) layer on the surface of electrode during the first charge/discharge step.[18,29] In addition, a large irreversible capacity loss was observed in the first cycle, which was attributed to the high surface area of the graphene sheets, as observed in many graphene-based materials.[41−43] After the second cycle, the Coulombic efficiency increased rapidly, with an average columbic efficiency of 99.47%. Figure 3b shows the voltage profiles of the Ge/RGO/C nanocomposites. During the charge process, the voltage decreased steeply from the open circuit voltage to 0.6 V, a plateau region sets in, and then the voltage further decreased slowly until ~0 V. In the discharge profile, a plateau can be clearly observed at 0.3 V. Figure 3c shows the differential capacity profiles of the first, second, and 10th cycles. The peaks indicate insertion of Li ions into equipotential sites, and the presence of sharp peaks in the first charge cycle suggests that different Li–Ge alloy phases were formed during lithiation. The lithiation peaks observed at approximately 0.1–0.3 and 0.3–0.5 V are consistent with those reported for galvanostatic cycling of Ge. During the subsequent charge cycles, there was only one peak at ~140 mV, implying that the capacity of the Ge/RGO/C electrode was mainly contributed by Ge. The discharge capacities of the second and 75th cycles were 1055 and 1166 mAh/g, respectively. The discharge capacity is maintained at ~100% without obvious fading at the 0.2 C rate. The RGO anode obtained from the synthesis

dx.doi.org/10.1021/cm5002016 | *Chem. Mater.* 2014, 26, 2172–2179

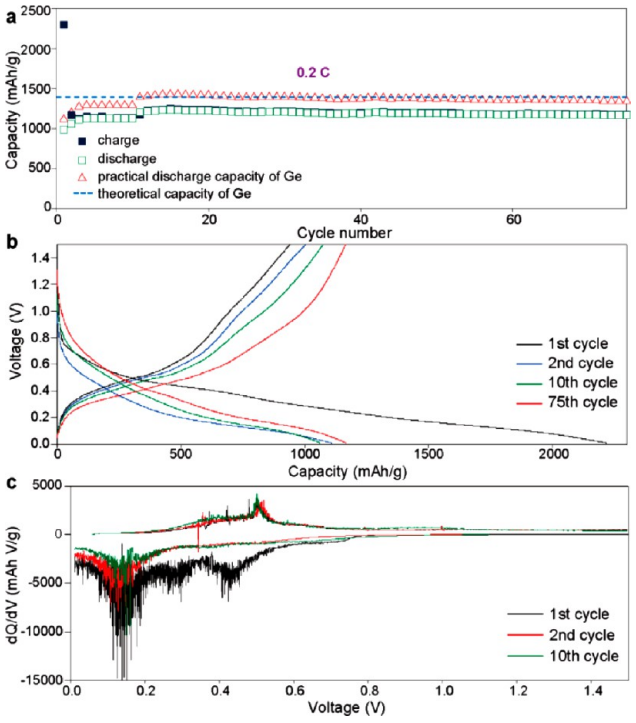

Figure 3. (a) Charge/discharge cycle performance of Ge/RGO/C nanocomposites at a rate of 0.2 C between 0.01 and 1.5 V. (b) Voltage profiles of the first, second, 10th, and 75th cycles. (c) Differential capacity profiles of the first, second, and 10th cycles of Ge/RGO/C composites.

delivers a reversible capacity of 550 mAh/g at a rate of 0.2 C (see Figure S4 in the Supporting Information). Thus, the practical capacity of Ge nanoparticles can be calculated, as shown in Figure 3a. On the basis of the estimated mass portion of Ge nanoparticles (79.32 wt %) in the electrode, the calculated reversible capacity of Ge nanoparticles was 1332 mAh/g, which is ~96.2% of the theoretical capacity of Ge (1384 mAh/g).

For Ge-based anodes, long-term stability when cycled at high charge and discharge rates is a significant challenge because of the dramatic volume changes owing to the insertion/extraction of Li ions. In most studies, the number of cycles at high charge rates (>1 C) is usually less than 100 for Ge-based anodes.[16,29,30,44−46] In this study, a cycling test over hundreds of cycles was carried out to examine the long-term stability of the electrodes at high charge/discharge rates. As shown in Figure 4a, the cycling test was carried out at a rate of 0.2 C for the first 20 cycles followed by a rate of 1 C for subsequent cycles. The charge- and discharge-specific capacities are 1042 and 972 mAh/g for the first cycle at the 1 C rate (the 21st cycle at Figure 4a), respectively. After 600 cycles, the discharge capacity (993 mAh/g) is maintained at ~100% without fading when compared to its initial capacity (972 mAh/g) at 1 C, suggesting excellent cycling stability. The inset of Figure 4a shows the voltage profiles that clearly illustrate that the charge and discharge capacities at the 600th cycle are very close to those at the 21st cycle. Figure 4b shows the results for the higher cycle rate of 2 C. The discharge capacity remains at 863 mAh/g for the first cycle at the 2 C rate (the 16th cycle in Figure 4b). After 300 cycles, the Ge/RGO/C nanocomposites still retain a reversible capacity of 780 mAh/g. The inset of Figure 4b shows the voltage profiles of the composite electrode

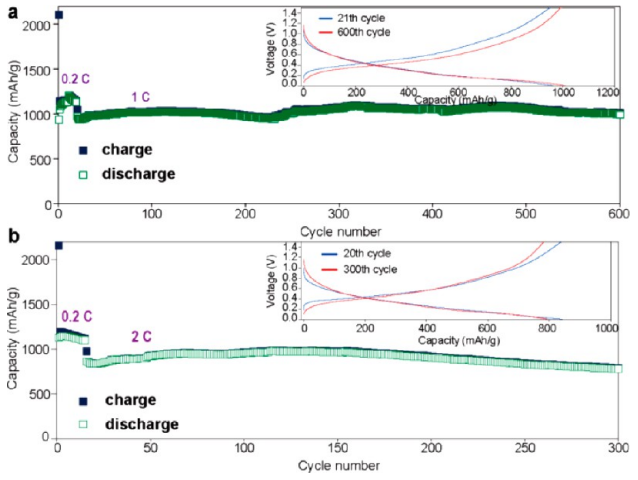

Figure 4. (a) Charge/discharge cycle performance of Ge/RGO/C nanocomposites cycled 600 times at a rate of 0.2 C for the initial 20 cycles followed by a rate of 1 C for subsequent cycles. The inset shows the voltage profiles of the 21st and 600th cycles. (b) Cycle performance of Ge/RGO/C nanocomposites cycled 300 times at a rate of 0.2 C for initial 15 cycles followed by cycling at a charge/discharge rate of 2 C. The inset shows the voltage profiles of the 20th and 300th cycles.

in the 0.01 V range versus Li/Li$^+$ at the 2 C rate, and the profiles are similar to those at the 0.2 C rate (Figure 3b). From the voltage profiles, the charge/discharge curves at the 20th and the 300th cycles almost overlap, indicating extremely stable electrode performance during the cycling tests.

For practical applications, the electrode needs to be examined over a wide range of operating rates, from low rates (0.2 to 1 C) to high rates (1 C to tens of C), and at high temperatures. As shown in Figure 5a, a 360-cycle test with rates

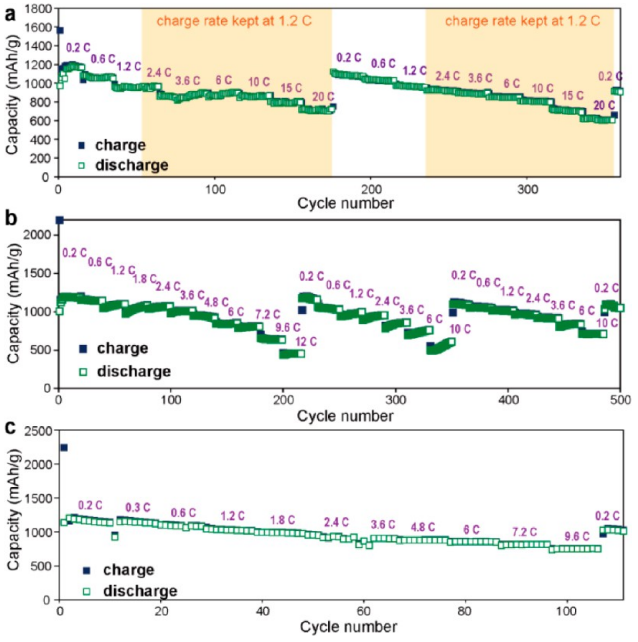

Figure 5. Rate capability of Ge/RGO/C nanocomposites. (a) Cycle performance of a 360-cycle test with discharge rates ranging from 0.2 to 20 C. (b) Cycle performance of a 500-cycle test with charge/discharge rates ranging from 0.2 to 12 C. (c) Cycle performance at different rates at 55 °C.

dx.doi.org/10.1021/cm5002016 | *Chem. Mater.* 2014, 26, 2172−2179

ranging from 0.2 to 20 C were conducted to evaluate the rate capabilities of the Ge/RGO/C nanocomposites. In the operation parameters, the charge/discharge rates can be divided into two parts. In the first regime (i.e., from 0.2 to 1.2 C), the charge and discharge rates were kept the same for each period. In the second regime (i.e., from 2.4 to 20 C), the discharge rate was changed for each period, but the charge rate was fixed at 1.2 C. The nanocomposites exhibited discharge capacities of 1166 (0.2 C), 1049 (0.6 C), 953 (1.2 C), 962 (2.4 C), 887 (3.6 C), 894 (6 C), 867 (10 C), 794 (15 C), and 720 mAh/g (20 C). The discharge capacity of 720 mAh/g at 20 C was 74.15% of the original capacity without a large fading when compared with its initial discharge capacity (971 mAh/g) at the 0.2 C rate. A specific discharge capacity of ~1100 mAh/g was quickly recovered when the charge/discharge rate was lowered again to 0.2 C after 350 cycles. Surprisingly, the remeasured discharge capacity is almost the same as the first few cycles. The detailed information for each period is listed in Table S2 in the Supporting Information. Moreover, cycling tests at the same charge and discharge rates to evaluate more comprehensive operating conditions were also carried out. As shown in Figure 5b, the anode was tested with 500 cycles to determine its capacity stability. During the cycling tests, the charge and discharge rates were kept the same for each period, and discharge capacities of 1182 (0.2 C), 1142 (0.6 C), 1101 (1.2 C), 1178 (1.8 C), 1071 (2.4 C), 1010 (3.6 C), 917 (4.8 C), 851 (6 C), 804 (7.2 C), 632 (9.6 C), and 453 mAh/g (12 C) were obtained. The discharge capacity of composites is 453 mAh/g at 12 C, which is still larger than the theoretical capacity of graphite. After the high-rate tests, the cycle rate was returned to 0.2 C, and the capacity recovered rapidly. A reversible capacity of approximately 1050 mAh/g was maintained after 500 cycles. Table S3 in the Supporting Information shows the detailed information of the cycle performance of nanocomposites at rates ranging from 0.2 to 12 C. The performance of the Ge/RGO/C anode tested over long cycles is better than or comparable with the different types of Ge nanostructures, such as thin films,[47,48] particles,[45,49−51] mesoporous,[52,53] nanowires,[16,18,54,55] nanotubes,[56,57] nanoparticles encapsulated with carbon,[58,59] and other graphene-based composites.[30,60] Moreover, the cycle performance of Ge/RGO/C was tested at 55 °C at charge/discharge rates ranging from 0.2 to 9.6 C with voltages ranging from 0.01 to 1.5 V to evaluate its thermal stability (Figure 5c). The electrode exhibited discharge capacities of 1131 (0.2 C), 1121 (0.6 C), 1080 (1.2 C), 1017 (1.8 C), 950 (2.4 C), 901 (3.6 C), 879 (4.8 C), 852 (6 C), 813 (7.2 C), and 750 mAh/g (9.6 C). The achieved capacities were similar to those obtained at room temperature at 0.2 C, thus demonstrating the high-temperature thermal stability of the electrode.

Moreover, the polycrystalline Ge nanoparticles on the RGO sheets were observed to transform to fine nanoparticles with an average size of 5 nm after the first cycle at the 1 C rate (Figure 6a). This particle size is similar to that of the Ge nanoparticles before carbonization. The excellent cycling performance of Ge/RGO/C can also be attributed to the stability of the Ge nanoparticles on the RGO sheets during the insertion/extraction of Li ions. However, the Ge nanoparticles detached immediately when Ge/RGO nanocomposites were cycled several times, resulting in poor performance (Figures S5 and S6 in the Supporting Information show the electrochemical performance and TEM images after cycling). Thus, the RGO/C sandwich structures offer the following benefits. First, Ge nanoparticles were encapsulated tightly between the RGO and a thin carbon-coating layer in the sandwich structures, thus effectively protecting the electrode structure during charge/discharge cycles. This structural toleration is crucial for maintaining the electrochemical performance of Ge nanoparticles. Second, the RGO not only prevents the adjacent Ge nanoparticles from coalescence but also provides much faster electron-transport channels because of their surface-to-surface contacts. Third, the elasticity of carbon covering both sides of the composites can effectively alleviate the pulverization derived from the volume change of Ge during the insertion/extraction of Li ions and prevent the Ge nanoparticles from falling off. Finally, the interstitial sites between the Ge nanoparticles provide sufficient space for the change of volume of Ge particles during Li−Ge alloying/dealloying reactions. The morphology of the Ge/RGO/C nanocomposite after hundreds of cycles was also studied to confirm the integrity of the Ge/RGO/C electrodes. Furthermore, the TEM images of the Ge/RGO/C after 500 cycles with different rates (Figure 6b) and after 600 cycles at a 1 C rate show similar structures that feature uniform Ge particles adhered to the RGO sheets (Figure 6c,d).

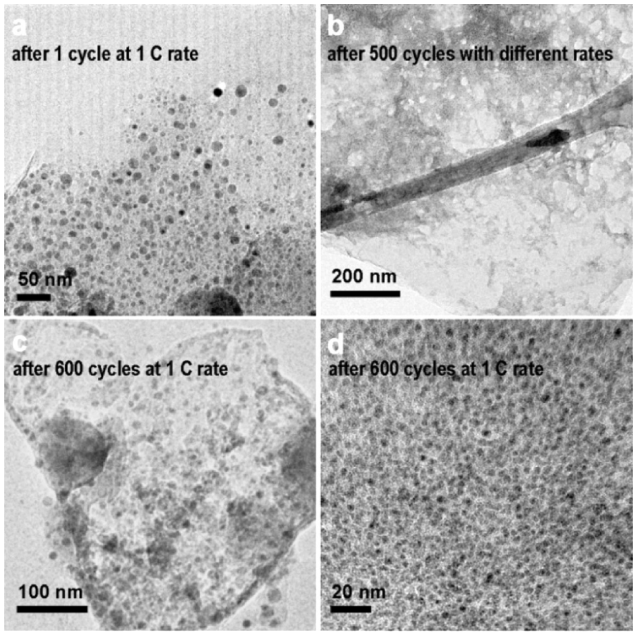

Figure 6. Structure evolution of Ge/RGO/C nanocomposites after charge/discharge cycles: (a) after 1 cycle at a 1 C rate, (b) after 500 cycles with different rates, and (c, d) after 600 cycles at a 1 C rate.

The calculated volumetric capacity of the RGO/Ge/C is around 700 mAh/cm^3 (the reversible capacity of 1166 mAh/g at a rate of 0.2 C; the weight, area, and thickness of the Ge/RGO/C electrode are 0.6 mg, 1 cm^2, and 10 μm, respectively). This value is higher than reported values of commercial graphite anodes (300−400 mAh/cm^3).[61,62] As shown in Figure 7, full cells with a Ge/RGO/C anode and an $LiCoO_2$ cathode were fabricated. The mass loadings of the cathode and the anode were approximately 7 and 0.6 mg/cm^2, respectively. The cathode material was loaded in excess to balance the irreversible capacity of the anode. Figure 7a shows the cycle performance of Ge/RGO/C in a CR2032-type coin full cell. The full cell exhibited a discharge capacity of 1234 mAh/g in the first cycle at a rate of 1 C between 2.5 and 4.2 V. The capacity obtained in the second cycle was reduced slightly because the capacity ratio of the anode/cathode was not optimized and because of the

dx.doi.org/10.1021/cm5002016 | Chem. Mater. 2014, 26, 2172−2179

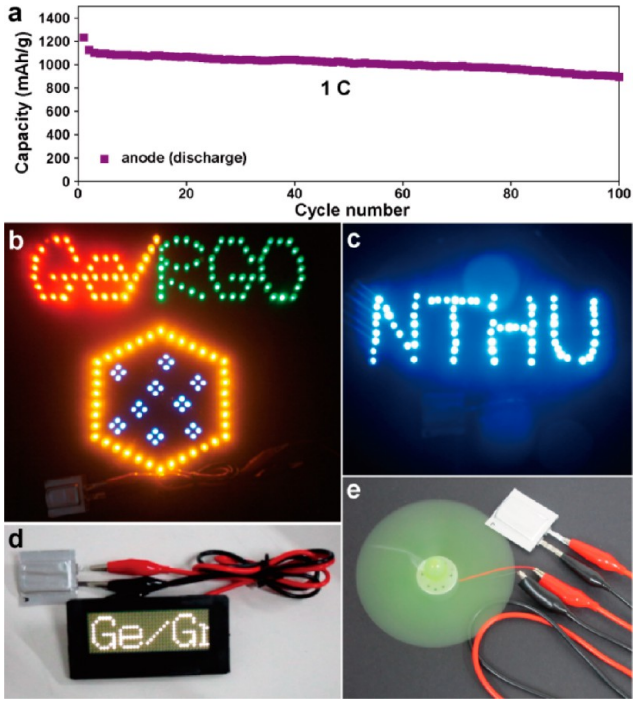

Figure 7. (a) Discharge capacity of the Ge/RGO/C anode versus cycle number in a full cell with an $LiCoO_2$ cathode at a charge/discharge rate of 1 C between 2.5 and 4.2 V. Aluminum-pouch-type Li-ion batteries were used to power different electronic devices, including (b) an LED array containing over 150 bulbs, (c) blue LED bulbs, (d) a scrolling LED marquee, and (f) an electric fan. Movies S1−S3 in the Supporting Information show the handling of the batteries with the Ge/RGO/C anode to power these electronic devices.

high irreversible capacity of the anode. However, the cell had a stable capacity of ∼1000 mAh/g in subsequent cycles, and the Ge/RGO/C anode still had a reversible discharge capacity of 900 mAh/g after 100 cycles. A larger Ge/RGO/C anode was built by incorporating it into an aluminum-pouch-type Li-ion battery, as shown in Scheme 1c. The size of the anode electrode used in the pouch-type Li-ion battery was about 3 × 15 cm^2. The mass loading at the anode/cathode in the pouch-type cell was similar to that of the CR2032-type coin cell, and the single battery offered a capacity of over 20 mAh. To the best of our knowledge, we are the first to incorporate graphene/Li-alloy anodes into a commercial cell-fabrication process. To facilitate Ge/RGO/C nanocomposite applications, a single battery was used to power different portable devices. A single battery was shown to power a scrolling LED marquee that displays "Ge/Graphene Composite Anodes for Lithium Ion Battery" (Figure 7d). Additionally, when connected to the battery, an electric fan rotated intensely (Figure 7e). Moreover, parallel connection of aluminum pouch-type Li-ion batteries can generate larger electric current, and the six parallel-connected cells provided a capacity of 120 mAh that can turn on over 150 5 mm (light-emitting-diode) LED bulbs to light intensely (Figure 7b). Commercial blue LED bulb arrays that need higher turn-on voltages can also be instantly turned on (Figure 7c). Movies showing the manipulation of cells to drive LED marquees, LED displays, and electric fans are provided in the Supporting Information.

4. CONCLUSIONS

High-nanoparticle-loading Ge/RGO/C nanocomposites were prepared in scalable solution-based reactions and shown to exhibit superior performance, such as a practical Ge capacity close to its theoretical value and a high rate capability over hundreds of cycles, as Li-ion anodes. In addition, their uses for many practical Li-ion battery applications were presented. Even though the RGO sheets are covered with a very high concentration of Ge particles, the nanoparticles retain their morphology when subjected to high-rate Li-alloying and -dealloying reactions. The thin carbon-coating layer plays an important role in encapsulating and confining the Ge particles on the RGO sheets, thus giving this Ge/RGO/C sandwich structure excellent electrochemical performance. Moreover, pouch-type full cells were successfully built using commercial fabrication processes to output a larger current (20 mAh) that was able to power a wide range of electronic devices. This study shows that graphene loaded with a large amount of nanoparticles has high potential for use in practical Li-ion battery applications because of its superior anode performance. In the future, a graphene-based battery system that can offer massive current and voltage may be realized with parallel-connected, series-connected, or parallel/series complex architectures for use in a wide range of applications.

■ ASSOCIATED CONTENT

Supporting Information

XRD, TEM images, CHNS analysis, Nyquist plots, and other galvanostatic charge/discharge profiles of the RGO, Ge/RGO, and Ge/RGO/C composites (PDF); movies showing electronic devices, including LED marquee, LED display, and electric fans powered by the Li-ion batteries (AVI). This material is available free of charge via the Internet at http://pubs.acs.org.

■ AUTHOR INFORMATION

Corresponding Author

*Tel.: + 886-3-572-3661. Fax: + 886-3-571-5408. E-mail: hytuan@che.nthu.edu.tw.

Notes

The authors declare no competing financial interest.

■ ACKNOWLEDGMENTS

We acknowledge the financial support from the National Science Council of Taiwan (NSC 102-2221-E-007-023-MY3, NSC 102-2221-E-007-090-MY2, NSC 101-2623-E-007-013-IT, and NSC102-2633-M-007-002), the Ministry of Economic Affairs, Taiwan (101-EC-17-A-09-S1-198), National Tsing Hua University (102N2051E1 and 102N2061E1), and the assistance from Center for Energy and Environmental Research, National Tsing-Hua University.

■ REFERENCES

(1) Marom, R.; Amalraj, S. F.; Leifer, N.; Jacob, D.; Aurbach, D. *J. Mater. Chem.* **2011**, *21*, 9938−9954.
(2) Scrosati, B.; Garche, J. *J. Power Sources* **2010**, *195*, 2419−2430.
(3) Tarascon, J. M.; Armand, M. *Nature* **2001**, *414*, 359−367.
(4) Cheng, F. Y.; Liang, J.; Tao, Z. L.; Chen, J. *Adv. Mater.* **2011**, *23*, 1695−1715.
(5) Guo, W.; Xue, X.; Wang, S.; Lin, C.; Wang, Z. L. *Nano Lett.* **2012**, *12*, 2520−2523.

(6) Deng, J. W.; Yan, C. L.; Yang, L. C.; Baunack, S.; Oswald, S.; Wendrock, H.; Mei, Y. F.; Schmidt, O. G. *ACS Nano* **2013**, *7*, 6948−6954.
(7) Lin, J.; Peng, Z. W.; Xiang, C. S.; Ruan, G. D.; Yan, Z.; Natelson, D.; Tour, J. M. *ACS Nano* **2013**, *7*, 6001−6006.
(8) Xin, X.; Zhou, X. F.; Wu, J. H.; Yao, X. Y.; Liu, Z. P. *ACS Nano* **2012**, *6*, 11035−11043.
(9) Xue, X.; Wang, S.; Guo, W.; Zhang, Y.; Wang, Z. L. *Nano Lett.* **2012**, *12*, 5048−5054.
(10) Mahmood, N.; Zhang, C.; Liu, F.; Zhu, J.; Hou, Y. *ACS Nano* **2013**, *7*, 10307−10318.
(11) Needham, S. A.; Wang, G. X.; Liu, H. K.; Drozd, V. A.; Liu, R. S. *J. Power Sources* **2007**, *174*, 828−831.
(12) Georgakilas, V.; Otyepka, M.; Bourlinos, A. B.; Chandra, V.; Kim, N.; Kemp, K. C.; Hobza, P.; Zboril, R.; Kim, K. S. *Chem. Rev.* **2012**, *112*, 6156−6214.
(13) Lee, S. W.; Gallant, B. M.; Byon, H. R.; Hammond, P. T.; Shao-Horn, Y. *Energy Environ. Sci.* **2011**, *4*, 1972−1985.
(14) Chockla, A. M.; Klavetter, K. C.; Mullins, C. B.; Korgel, B. A. *ACS Appl. Mater. Interfaces* **2012**, *4*, 4658−4664.
(15) Park, C. M.; Kim, J. H.; Kim, H.; Sohn, H. J. *Chem. Soc. Rev.* **2010**, *39*, 3115−3141.
(16) Chan, C. K.; Zhang, X. F.; Cui, Y. *Nano Lett.* **2008**, *8*, 307−309.
(17) Seng, K. H.; Park, M. H.; Guo, Z. P.; Liu, H. K.; Cho, J. *Angew. Chem., Int. Ed.* **2012**, *51*, 5657−5661.
(18) Yuan, F. W.; Yang, H. J.; Tuan, H. Y. *ACS Nano* **2012**, *6*, 9932−9942.
(19) Chan, C. K.; Peng, H. L.; Liu, G.; McIlwrath, K.; Zhang, X. F.; Huggins, R. A.; Cui, Y. *Nat. Nanotechnol.* **2008**, *3*, 31−35.
(20) Deb-Choudhury, S.; Prabakar, S.; Krsinic, G.; Dyer, J. M.; Tilley, R. D. *J. Agric. Food Chem.* **2013**, *61*, 7188−7194.
(21) Warner, J. H.; Tilley, R. D. *Nanotechnology* **2006**, *17*, 3745−3749.
(22) Geaney, H.; Mullane, E.; Ryan, K. M. *J. Mater. Chem. C* **2013**, *1*, 4996−5007.
(23) Barrett, C. A.; Singh, A.; Murphy, J. A.; O'Sullivan, C.; Buckley, D. N.; Ryan, K. M. *Langmuir* **2011**, *27*, 11166−11173.
(24) Hanrath, T.; Korgel, B. A. *J. Am. Chem. Soc.* **2002**, *124*, 1424−1429.
(25) Tuan, H. Y.; Lee, D. C.; Hanrath, T.; Korgel, B. A. *Chem. Mater.* **2005**, *17*, 5705−5711.
(26) Lu, X. M.; Korgel, B. A.; Johnston, K. P. *Chem. Mater.* **2005**, *17*, 6479−6485.
(27) Liang, W.; Yang, H.; Fan, F.; Liu, Y.; Liu, X. H.; Huang, J. Y.; Zhu, T.; Zhang, S. *ACS Nano* **2013**, *7*, 3427−3433.
(28) Prabakar, S.; Shiohara, A.; Hanada, S.; Fujioka, K.; Yamamoto, K.; Tilley, R. D. *Chem. Mater.* **2010**, *22*, 482−486.
(29) Xue, D. J.; Xin, S.; Yan, Y.; Jiang, K. C.; Yin, Y. X.; Guo, Y. G.; Wan, L. J. *J. Am. Chem. Soc.* **2012**, *134*, 2512−2515.
(30) Cheng, J. S.; Du, J. *CrystEngComm* **2012**, *14*, 397−400.
(31) Sun, Y. M.; Hu, X. L.; Luo, W.; Huang, Y. H. *J. Phys. Chem. C* **2012**, *116*, 20794−20799.
(32) Bai, H.; Li, C.; Shi, G. Q. *Adv. Mater.* **2011**, *23*, 1089−1115.
(33) Zhi, L. J.; Fang, Y.; Kang, F. Y. *New Carbon Mater.* **2011**, *26*, 5−8.
(34) Liang, M. H.; Zhi, L. J. *J. Mater. Chem.* **2009**, *19*, 5871−5878.
(35) Wu, Z. S.; Ren, W. C.; Wen, L.; Gao, L. B.; Zhao, J. P.; Chen, Z. P.; Zhou, G. M.; Li, F.; Cheng, H. M. *ACS Nano* **2010**, *4*, 3187−3194.
(36) Chockla, A. M.; Panthani, M. G.; Holmberg, V. C.; Hessel, C. M.; Reid, D. K.; Bogart, T. D.; Harris, J. T.; Mullins, C. B.; Korgel, B. A. *J. Phys. Chem. C* **2012**, *116*, 11917−11923.
(37) Yang, H. J.; Tuan, H. Y. *J. Mater. Chem.* **2012**, *22*, 2215−2225.
(38) Xue, D. J.; Wang, J. J.; Wang, Y. Q.; Xin, S.; Guo, Y. G.; Wan, L. J. *Adv. Mater.* **2011**, *23*, 3704−3707.
(39) Pang, D. W. P.; Yuan, F. W.; Chang, Y. C.; Li, G. A.; Tuan, H. Y. *Nanoscale* **2012**, *4*, 4562−4570.
(40) Su, Y. Z.; Li, S.; Wu, D. Q.; Zhang, F.; Liang, H. W.; Gao, P. F.; Cheng, C.; Feng, X. L. *ACS Nano* **2012**, *6*, 8349−8356.
(41) Luo, B.; Wang, B.; Li, X. L.; Jia, Y. Y.; Liang, M. H.; Zhi, L. J. *Adv. Mater.* **2012**, *24*, 3538−3543.
(42) Wang, X.; Cao, X. Q.; Bourgeois, L.; Guan, H.; Chen, S. M.; Zhong, Y. T.; Tang, D. M.; Li, H. Q.; Zhai, T. Y.; Li, L.; Bando, Y.; Golberg, D. *Adv. Funct. Mater.* **2012**, *22*, 2682−2690.
(43) Zhang, C. F.; Peng, X.; Guo, Z. P.; Cai, C. B.; Chen, Z. X.; Wexler, D.; Li, S.; Liu, H. K. *Carbon* **2012**, *50*, 1897−1903.
(44) DiLeo, R. A.; Frisco, S.; Ganter, M. J.; Rogers, R. E.; Raffaelle, R. P.; Landi, B. J. *J. Phys. Chem. C* **2011**, *115*, 22609−22614.
(45) Lee, H.; Kim, M. G.; Choi, C. H.; Sun, Y. K.; Yoon, C. S.; Cho, J. *J. Phys. Chem. B* **2005**, *109*, 20719−20723.
(46) Seo, M. H.; Park, M.; Lee, K. T.; Kim, K.; Kim, J.; Cho, J. *Energr Environ. Sci.* **2011**, *4*, 425−428.
(47) Laforge, B.; Levan-Jodin, L.; Salot, R.; Billard, A. *J. Electrochem. Soc.* **2008**, *155*, A181−A188.
(48) Abel, P. R.; Chockla, A. M.; Lin, Y. M.; Holmberg, V. C.; Harris, J. T.; Korgel, B. A.; Heller, A.; Mullins, C. B. *ACS Nano* **2013**, *7*, 2249−2257.
(49) Klavetter, K. C.; Wood, S. M.; Lin, Y. M.; Snider, J. L.; Davy, N. C.; Chockla, A. M.; Romanovicz, D. K.; Korgel, B. A.; Lee, J. W.; Heller, A.; Mullins, C. B. *J. Power Sources* **2013**, *238*, 123−136.
(50) Cho, Y. J.; Im, H. S.; Kim, H. S.; Myung, Y.; Back, S. H.; Lim, Y. R.; Jung, C. S.; Jang, D. M.; Park, J.; Cha, E. H.; Cho, W. I.; Shojaei, F.; Kang, H. S. *ACS Nano* **2013**, *7*, 9075−9084.
(51) Cho, Y. J.; Im, H. S.; Myung, Y.; Kim, C. H.; Kim, H. S.; Back, S. H.; Lim, Y. R.; Jung, C. S.; Jang, D. M.; Park, J.; Cha, E. H.; Choo, S. H.; Song, M. S.; Cho, W. I. *Chem. Commun.* **2013**, *49*, 4661−4663.
(52) Yang, L. C.; Gao, Q. S.; Li, L.; Tang, Y.; Wu, Y. P. *Electrochem. Commun.* **2010**, *12*, 418−421.
(53) Wang, X. L.; Han, W. Q.; Chen, H. Y.; Bai, J. M.; Tyson, T. A.; Yu, X. Q.; Wang, X. J.; Yang, X. Q. *J. Am. Chem. Soc.* **2011**, *133*, 20692−20695.
(54) Tan, L. P.; Lu, Z. Y.; Tan, H. T.; Zhu, J. X.; Rui, X. H.; Yan, Q. Y.; Hng, H. H. *J. Power Sources* **2012**, *206*, 253−258.
(55) Mullane, E.; Kennedy, T.; Geaney, H.; Dickinson, C.; Ryan, K. M. *Chem. Mater.* **2013**, *25*, 1816−1822.
(56) Park, M. H.; Cho, Y.; Kim, K.; Kim, J.; Liu, M. L.; Cho, J. *Angew. Chem., Int. Ed.* **2011**, *50*, 9647−9650.
(57) Cui, G. L.; Gu, L.; Kaskhedikar, N.; van Aken, P. A.; Maier, J. *Electrochim. Acta* **2010**, *55*, 985−988.
(58) Cui, G. L.; Gu, L.; Zhi, L. J.; Kaskhedikar, N.; van Aken, P. A.; Mullen, K.; Maier, J. *Adv. Mater.* **2008**, *20*, 3079−3083.
(59) Yoon, S.; Park, C. M.; Sohn, H. J. *Electrochem. Solid-State Lett.* **2008**, *11*, A42−A45.
(60) Ren, J. G.; Wu, Q. H.; Tang, H.; Hong, G.; Zhang, W. J.; Lee, S. T. *J. Mater. Chem. A* **2013**, *1*, 1821−1826.
(61) Manthiram, A.; Applestone, D. *RSC Adv.* **2012**, *2*, 5411−5417.
(62) Jeong, S.; Lee, J. P.; Ko, M.; Kim, G.; Park, S.; Cho, J. *Nano Lett.* **2013**, *13*, 3403−3407.